Variational segmentation model with non-local image dehazing for boundary extraction in vector-valued hazy images

ⓘ **Salma Huda Ahmad Mahizan[1]**
ⓘ **Nur Nabihah Shafee[2]**
ⓘ **Abdul Kadir Jumaat[1,3+]**

[1,2]*Faculty of Computer and Mathematical Sciences, Universiti Teknologi MARA, 40450 Shah Alam, Malaysia.*
[1]*Email: salmahudapx@gmail.com*
[2]*Email: bihahshfe@gmail.com*
[3]*Institute for Big Data Analytics and Artificial Intelligence (IBDAAI), Kompleks Al-Khawarizmi, Universiti Teknologi MARA, 40450, Shah Alam, Selangor, Malaysia.*
[3]*Email: abdulkadir@tmsk.uitm.edu.my*

(+ Corresponding author)

ABSTRACT

Image segmentation is a fundamental technique for delineating boundaries within images, enabling detailed analysis and simplifying subsequent processing tasks. Recently, a variational selective segmentation model for vector-valued (color) images, termed Selective Segmentation based on Gaussian Regularization (SSGR), was introduced. In this variational model, the standard regularization term is replaced with a Gaussian function, yielding a speed improvement of approximately 247 times compared with the earlier formulation, while maintaining comparable accuracy. However, the SSGR model shows limitations when applied to hazy images. To address this, the present study reformulates the SSGR model by incorporating Non-Local Image Dehazing as the new fitting term, resulting in a modified approach named Selective Segmentation for Haze Image (SSHI). Experiments were conducted on hazy images to evaluate the proposed model. The performance of SSHI was assessed using common segmentation metrics: Error, Accuracy (ACU), Jaccard Similarity Coefficient (JSC), and Dice Similarity Coefficient (DSC). Efficiency was measured by recording processing time. Numerical experiments demonstrated that the SSHI model, through the integration of Non-Local Image Dehazing, consistently achieved the highest ACU, JSC, and DSC values, while also yielding the lowest Error and processing time compared to existing methods. These findings confirm that SSHI provides improved accuracy and efficiency for hazy image segmentation. The proposed model has potential applications in domains where hazy imaging is common, including medical imaging such as X-ray and endoscopy, remote sensing, and environmental surveillance. Future research may extend this framework to three-dimensional formulations for more complex imaging applications.

Contribution/Originality: This study contributes a novel extension of the SSGR model by integrating Non-Local Image Dehazing, forming the SSHI model. The originality lies in addressing segmentation under hazy conditions, with demonstrated improvements in accuracy and efficiency, offering practical applications in environmental, medical, and remote sensing imaging.

1. INTRODUCTION

Image processing is the technique of analyzing and manipulating images to extract meaningful information, thereby making them easier to interpret or utilize. It is one of the most influential technological innovations of modern times, with applications ranging from satellite communications and mobile imaging to medical diagnostics. The outcomes of image processing directly influence higher-level tasks such as image recognition and interpretation.

Image processing can be broadly categorized into analogue and digital methods. Among these, digital image processing plays a central role, particularly in boundary extraction, a critical step for further analysis that is commonly referred to as image segmentation. Image segmentation has diverse applications, including medical image analysis [1-5], pattern recognition, image understanding, and computer vision [6, 7].

Image segmentation divides an image into regions or objects by extracting boundaries, thereby simplifying subsequent analysis Mohd Ghani and Jumaat [8]. This process assigns labels to pixels, grouping them according to shared characteristics such as intensity, color, or texture. Segmentation approaches are generally divided into variational and non-variational models. Variational models are not dependent on the amount of data, less sensitive to noise, more feature-rich, and more effective in extracting homogeneous regions compared to non-variational approaches [9]. Within variational segmentation, global and selective segmentation techniques are the most prominent [8]. Global segmentation attempts to partition all objects in an image based on their statistical properties, but it is sensitive to noise, contrast, and illumination. Examples of global segmentation include the models proposed by Fang et al. [7], Gu, et al. [10], Yang, et al. [11], Iqbal, et al. [12] and Zhi and Shen [13]. In contrast, selective segmentation focuses on segmenting only user-defined target objects, making it preferable when analysis requires isolating specific structures. Applications suitable for the incorporation of selective segmentation techniques include research fields such as imaging [14, 15], biometric recognition [16], and processing of text [17].

Several selective segmentation models have been proposed. In Badshah and Chen [18] a new selective segmentation formulation was proposed by combining the idea of global segmentation with geometrical constraints. Later, Nguyen, et al. [19] proposed an Interactive Image Segmentation (IIS) model using two sets of geometric constraints, though later works [20] demonstrated that a single constraint was often more effective, albeit computationally expensive. Spencer and Chen [21] introduced the Distance Selective Segmentation (DSS) model, which reduces sensitivity to user input and computational burden. However, if the input data is a vector-valued (color) image, the DSS model would turn the input image into a grayscale image and discard the color information. A vector-valued (colored) image is typically a 24-bit image with 8 bits for red, 8 bits for green, and 8 bits for blue information. Vector-valued images, which include more information than grayscale images, produce more effective results for image segmentation, according to research by Mohd Ghani and Jumaat [8].

In order to obtain suitable segmentation results when segmenting vector-valued images, Mohd Ghani and Jumaat [8] proposed a Distance Selective Segmentation 2 (DSS2) model. However, the DSS2 model has a high computational cost since the usual regularization term used in the formulation results in the curvature term, which must be solved. To address this issue, Jumaat, et al. [22] reformulated DSS2 by replacing the traditional curvature regularization with a simpler Gaussian function. This led to the Selective Segmentation based on Gaussian Regularization (SSGR) model, which was nearly 247 times faster while maintaining comparable accuracy. Nevertheless, both DSS2 and SSGR perform poorly when applied to hazy images, where suspended particles (dust, fog, smoke) obscure details and degrade visibility [23]. This demonstrates the significance of the image dehazing process for real images. Haze removal, or image dehazing, aims to restore scene radiance by reducing atmospheric interference. However, existing techniques face challenges such as halo effects, color distortions, edge degradation, and blocking artifacts. Among various approaches, Non-Local Image Dehazing [24] has demonstrated high precision by simultaneously recovering haze-free images and distance maps.

Building on this, this study reformulates the SSGR model by substituting its fitting term with Non-Local Image Dehazing. The resulting model, termed Selective Segmentation for Haze Image (SSHI), is designed specifically for extracting the boundaries of vector-valued hazy images. Unlike earlier selective segmentation methods that rely mainly on global intensity information or simplified regularization terms, the SSHI model incorporates Non-Local Dehazing as part of the variational fitting energy itself. This design allows the segmentation to adapt directly to haze effects within the mathematical framework, instead of treating haze removal as a separate pre-processing step. By

combining information from both the original hazy image and its dehazed counterpart, SSHI introduces an approach that is not present in previous models.

2. REVIEW OF THE RELATED MODEL

In recent years, several deep learning methods have been introduced to address the challenge of segmenting images captured under fog or haze. Researchers [25] proposed a fog-invariant feature learning strategy to make semantic segmentation models more robust under low-visibility conditions. The authors Bi, et al. [26] later designed a frequency-decoupling method that separates amplitude and phase information in the Fourier domain to improve generalization to unseen fog. In a related study, the same authors, Bi, et al. [27] presented a bi-directional wavelet guidance framework for foggy-scene segmentation. Although these methods report strong results, their complexity and reliance on large and diverse training datasets remain major concerns.

More recently, Lee, et al. [25] explored a "fog-free training" strategy, where models are trained only on clear images but adapted for foggy environments. While this approach reduces the need for fog-specific training data, its performance still depends strongly on the scale of training data and network design. In addition, all of these methods in Lee, et al. [25], Bi, et al. [26], Bi, et al. [27] and Lee, et al. [28] follow a global segmentation paradigm in which all objects in an image are segmented. When the aim is to isolate a particular object of interest, selective segmentation approaches provide a more reliable solution.

A new selective segmentation approach for vector-valued images, termed Distance Selective Segmentation 2 (DSS2), was introduced in Mohd Ghani and Jumaat [8]. On image z_0, geometrical points $m_1 (\geq 3)$ were assumed by the marker set $B_0 = \{w_k = (x_k^*, y_k^*) \in \Omega, 1 \leq k \leq m_1\}$. The polygon P was constructed by using a set B_0. Let the function $P_d(x, y)$ be the Euclidean distance, which is the distance of each point $(x, y) \in \Omega$ from its nearest points of $(x_p, y_p) \in P$ constructed from the user input set B_0 defined as the following Equation 1.

$$P_d(x,y) = \sqrt{(x - x_p)^2 + (y - y_p)^2} \quad (1)$$

Then, the proposed DSS2 model is defined as the following Equation 2.

$$DSS2(\beta, d_1^i, d_2^i) = \mu \text{Length}(\beta) + \int_{inside(\beta)} \frac{1}{N} \sum_{i=1}^{N} \lambda_1^i \left(z_0^i(x,y) - d_1^i\right)^2 d\Omega$$
$$+ \int_{outside(\beta)} \frac{1}{N} \sum_{i=1}^{N} \lambda_2^i \left(z_0^i(x,y) - d_2^i\right)^2 d\Omega + \int_{inside(\beta)} \theta P_d(x,y) d\Omega, \quad (2)$$

where d_1^i and d_2^i are unknown constants that represent the average value of z_0^i inside and outside the unknown curve, respectively. The non-negative parameters of θ, μ, λ_1^i and λ_2^i are weights for the distance function, regularizing term and fitting term, respectively. Here, N is the number of channels. For color image, $N = 3$. Then, by introducing the level set function $\phi(x, y)$, Equation 2 can be written as the following Equation 3.

$$\min_{\phi, d_1^i, d_2^i} DSS2^{LS}(\phi, d_1^i, d_2^i),$$
$$DSS2^{LS}(\phi, d_1^i, d_2^i) = \mu \int_{\Omega} \delta(\phi)|\nabla\phi| d\Omega + \int_{\Omega} \frac{1}{N} \sum_{i=1}^{N} \lambda_2^i (1 - H(\phi))(z_0^i - d_2^i)^2 d\Omega \quad (3)$$
$$+ \int_{\Omega} \frac{1}{N} \sum_{i=1}^{N} \lambda_1^i H(\phi)(z_0^i - d_1^i)^2 d\Omega + \int_{\Omega} \theta H(\phi) P_d d\Omega,$$

where the Heaviside function, H and the Dirac delta function, δ were introduced. The functions $\phi(x, y), P_d(x, y)$ and $z_0^i(x, y)$ are replaced with ϕ, P_d and z_0^i respectively for simplicity and $|\nabla\phi| = \sqrt{\phi_x^2 + \phi_y^2}$. They fixed the function and minimized Equation 3 to obtain d_1^i and d_2^i as defined as the following Equation 4 and 5, respectively.

$$d_1^i(\phi) = \frac{\int_{\Omega} z_0^i H(\phi) dx dy}{\int_{\Omega} H(\phi) dx dy} (\text{average}(z_0^i) \text{on} \phi \geq 0) \quad (4)$$

$$d_2^i(\phi) = \frac{\int_{\Omega} z_0^i (1 - H(\phi)) dx dy}{\int_{\Omega} H(\phi) dx dy} (\text{average}(z_0^i) \text{on} \phi < 0) \quad (5)$$

To solve Equation 3, the Euler-Lagrange (EL) equation for ϕ is derived. Then, by fixing a constant d_1^i and d_2^i, the EL equation with respect to ϕ is given by the following Equation 6.

$$\begin{cases} \frac{\partial \phi}{\partial t} = \delta(\phi)\left[\mu\,\text{div}\left(\frac{\nabla\phi}{|\nabla\phi|}\right) - \frac{1}{N}\sum_{i=1}^{N}\lambda_1^i\left(z_0^{\ i} - d_1^i\right) + \frac{1}{N}\sum_{i=1}^{N}\lambda_2^i\left(z_0^{\ i} - d_2^i\right) - \theta P_d\right] \text{in } \Omega, \\ \frac{\delta(\phi)}{|\nabla\phi|}\frac{\partial \phi}{\partial \overrightarrow{m}} = 0 \qquad\qquad \text{on } \partial\Omega, \end{cases} \tag{6}$$

Where $\overrightarrow{m}$ is the exterior normal at the boundary of $\partial\Omega$ and $\frac{\partial \phi}{\partial \overrightarrow{m}}$ is the normal derivative of ϕ at the boundary. The finite differences scheme was used to solve this EL equation problem. Here, the curvature term, $\text{div}(\nabla\phi/|\nabla\phi|)$ that is derived from the total variation term, $|\nabla\phi|$ is highly nonlinear and results in high computational complexity. Consequently, the DSS2 model's segmentation procedure is slow.

To overcome the problem, researchers in Jumaat, et al. [22] introduced a new selective segmentation approach for a vector-valued image called Selective Segmentation Based on Gaussian Regularization (SSGR). The proposed model is then defined as the following Equation 7.

$$\min_{\phi^n, d_1^i, d_2^i} SSGR(\phi^n, d_1^i, d_2^i) = \int_{\Omega} \frac{1}{N}\sum_{i=1}^{N}\left(1 - H(\phi^n)\right)\left(z_0^i - d_2^i\right)^2 d\Omega +$$
$$\int_{\Omega} \frac{1}{N}\sum_{i=1}^{N} H(\phi^n)\left(z_0^i - d_1^i\right)^2 dD + \int_{\Omega} \theta H(\phi^n)P_d \, d\Omega \tag{7}$$
$$s.t \; \phi^{n+1} = \phi^n * G(x,y)$$

Gaussian function, $G(x,y)$ is used and defined as $G(x,y) = e^{-((x^2+y^2)/2)}$. The symbol $*$ is a convolution operator of the current solution ϕ with the Gaussian function, $G(x,y)$ and n indicates the number of iterations. Notice that in Equation 7, the total variation term, $|\nabla\phi|$ is removed and it is substituted with a Gaussian function as a regularizer to smooth the segmentation contour. Euler Euler-Lagrange equation is derived to solve Equation 7 as stated in the following Equation 8.

$$-\delta(\phi^n)\left[\frac{1}{N}\sum_{i=1}^{N}\left(\left(z_0^i - d_2^i\right)^2 - \left(z_0^i - d_1^i\right)^2 - \theta P_d\right)\right] = 0 \tag{8}$$

To solve Euler's Lagrange Equation 8, the gradient descent flow of Equation 8 is applied, and it is defined as follows.

$$\frac{\partial \phi}{\partial t} = \delta(\phi^n)\left[\frac{1}{N}\sum_{i=1}^{N}\left(\left(z_0^i - d_2^i\right)^2 - \left(z_0^i - d_1^i\right)^2 - \theta P_d\right)\right] \tag{9}$$

Notice that the curvature term is not involved in Equation 9 of the SSGR model, which results in less computational complexity compared to the original DSS2 model. However, the SSGR model performs less effectively when segmenting images with haze. Therefore, modifications to the SSGR model are necessary to improve its segmentation accuracy. The following section demonstrates the methodology to modify the SSGR model by employing image dehazing techniques.

3. METHODOLOGY

In this section, we present the development of a new modified model. Since the SSGR model was not designed to segment vector-valued images affected by haze, the main objective of this research is to effectively address this limitation. To achieve this, we introduce a new model, termed Selective Segmentation for Haze Image (SSHI), which integrates concepts from the SSGR model with the Non-Local Image Dehazing method proposed by Berman and Avidan [24]. According to Berman and Avidan [24], the dehaze image is computed using Equation 10:

$$\bar{z}_0^i = \frac{\{h_0^i - [1 - \hat{t}\,]L\}}{\hat{t}} \tag{10}$$

Where h_0^i is the input hazy image, $\hat{t}$ is the transmission medium, L is the air light in images and $\bar{z}_0^i$ is the output of Non-Local Image dehazing, which is the dehaze image. We incorporate the new fitting term $\bar{z}$ produced by the Non-Local Image Dehazing model into the SSGR model. Thus, the proposed model (SSHI) is formulated as follows.

$$\min_{\phi^n, d_1^i, d_2^i} SSHI = \frac{\alpha_1}{2N} \int_\Omega \sum_{i=1}^{N} H(\phi^n)(h_0^i - d_1^i)^2 \, d\Omega +$$

$$\frac{\alpha_1}{2N} \int_\Omega \sum_{i=1}^{N}(1 - H(\phi^n))(h_0^i - d_2^i)^2 \, d\Omega + \frac{\alpha_2}{2N} \int_\Omega \sum_{i=1}^{N} H(\phi^n)(\bar{z}_0^i - d_1^i)^2 \, d\Omega \quad (11)$$

$$+\frac{\alpha_2}{2N} \int_\Omega \sum_{i=1}^{N}(1 - H(\phi^n))(\bar{z}_0^i - d_2^i)^2 \, d\Omega + \int_\Omega \theta P_d \cdot H(\phi^n) d\Omega.$$

$$s.t \ \phi^{n+1} = \phi^n * G(x, y)$$

Notice that in Equation 11, the first two terms represent the fitting term that incorporates information from the original hazy image, h_0^i, weighted by the parameter α_1. The third and fourth terms correspond to the fitting term that utilizes information from the dehazed image, $\bar{z}_0^i$, weighted by the parameter α_2. In most cases, $\alpha_2 > \alpha_1$ ensuring that the SSHI model is capable of correctly identifying the object boundary. The final term is the distance term, which ensures that the targeted object is segmented successfully. At each iteration n, the segmentation curve ϕ, representing the image boundary, is convolved with a Gaussian function $G(x, y) = e^{-((x^2+y^2)/2)}$ to smooth the evolving curve. To solve Equation 11, the gradient descent flow of the Euler-Lagrange equation for the SSHI model is defined as the following Equation 12.

$$\frac{\partial \phi}{\partial t} = \delta(\phi^n) \left[\frac{\alpha_1}{N} \sum_{i=1}^{N} \left((h_0^i - d_2^i)^2 - (h_0^i - d_1^i)^2 \right) \right] +$$

$$\delta(\phi^n) \left[\frac{\alpha_2}{N} \sum_{i=1}^{N} \left((\bar{z}_0^i - d_2^i)^2 - (\bar{z}_0^i - d_1^i)^2 \right) \right] + \delta(\phi^n)[\theta P_d]. \quad (12)$$

Here, $\partial \phi / \partial t = (\phi^{n+1} - \phi^n) / \delta t$ denoted as the evolution of ϕ with respect to time t. In other words, the solution for the SSHI model is obtained by solving its associated Equation 12.

3.1. Algorithm for the Proposed Model

The implementation of the new model, namely, Selective Segmentation for Haze Image (SSHI), is summarized according to the following algorithm. All the parameters and algorithms will be configured and displayed here:

Algorithm SSHI: Algorithm to implement the SSHI Model

1. Set the tolerance, $tol = 0.00001$ and the maximum iterations, $maxit = 100$ as the stopping criteria. Set the parameter value of θ and define the marker set B_0.
2. Initialize $\phi^0, n = 0$.
3. Determine the average intensity region by computing ϕ and d_2^i in Equation 11.
4. To obtain ϕ^{n+1}, solve equation 12.
5. To regularize ϕ, convolve ϕ^{n+1} with the Gaussian function $G(x, y) = e^{-((x^2+y^2)/2)}$ such that $\phi^{n+1} = \phi^n * G(x, y)$.
6. If maximum iterations, $maxit = 100$ or $\|\phi^{r+1} - \phi^r\| / \|\phi^r\| \le tol$ then stop. Otherwise, repeat Steps 3 to 6.

In the numerical experiment, all images were resized to 128 x 128. The area parameter θ was employed to restrict segmentation to specific objects and was adjusted for each case according to the targeted item. A large value of θ should be used when the object is close to an adjacent boundary, whereas a smaller value of θ is preferable when the object is clearly separated. However, if θ is set too high, the final output may degenerate into a polygon. Satisfactory segmentation results can be achieved by selecting an appropriate value of θ together with marker points. For the SSHI model, the parameter θ was set in the range $\theta = [350,3600]$. In most cases, $\alpha_2 > \alpha_1$, which ensures
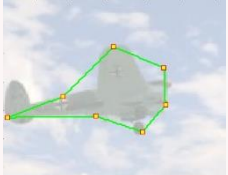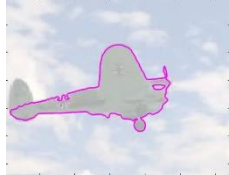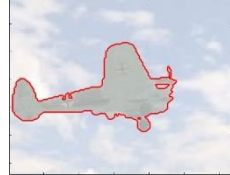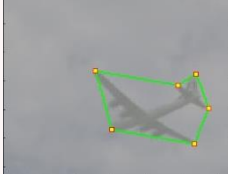
that the SSHI model is capable of correctly identifying object boundaries. The recommended range for α_1 and α_2 was [1,5]. The method was implemented in MATLAB.

Two methodologies were employed to evaluate the segmentation performance of the proposed model. The first was a qualitative approach, which assessed segmentation performance through visual observation. The second was a quantitative approach, which measured performance using the Jaccard Similarity Coefficient (JSC), Dice Similarity Coefficient (DSC), Accuracy (ACC), and Error. The values of JSC, DSC, ACC, and Error range between 0 and 1. For JSC, DSC, and ACC, values closer to 1 indicate higher segmentation accuracy, whereas for Error, values closer to 0 reflect better segmentation results. All values obtained for the proposed SSHI model were compared against those of existing models, namely DSS2 and SSGR. To evaluate processing efficiency, the tic and toc functions in MATLAB were used. The *tic* command initiates a stopwatch timer, while the *toc* command terminates it, records the elapsed time, and displays the result in seconds. This procedure was repeated three times to ensure consistency, and the average values of JSC, DSC, ACC, Error, and processing time were calculated.
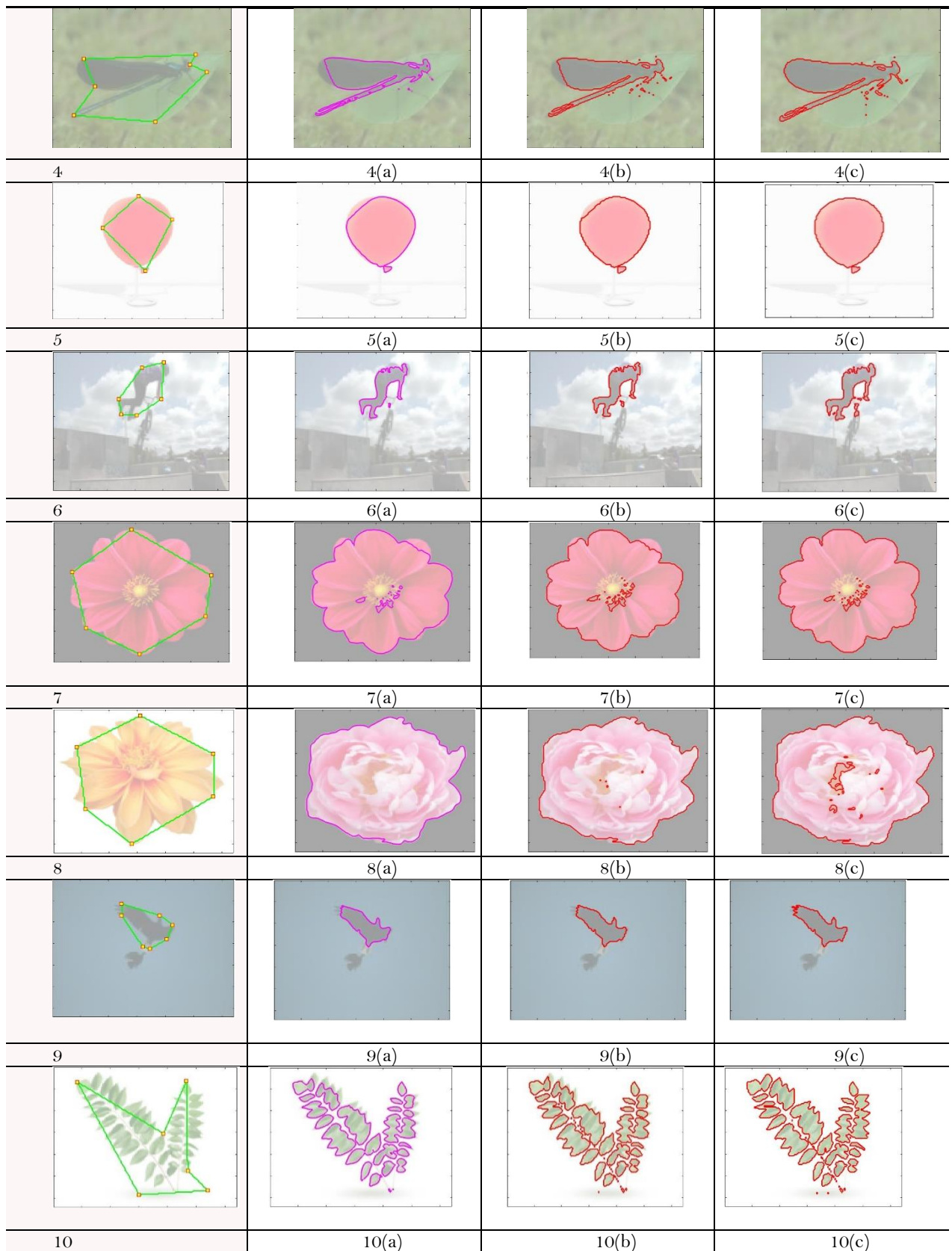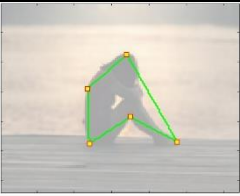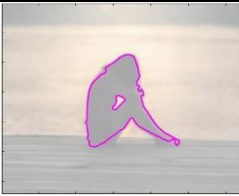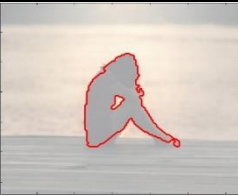
4. RESULTS AND DISCUSSION
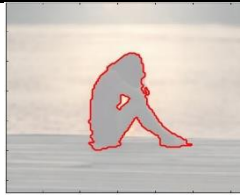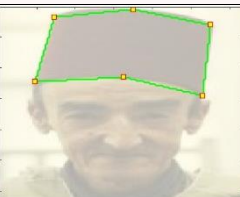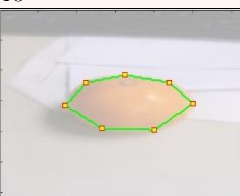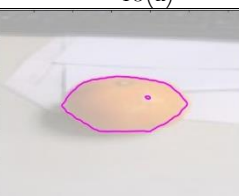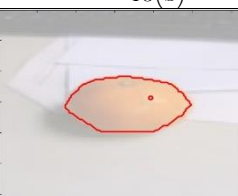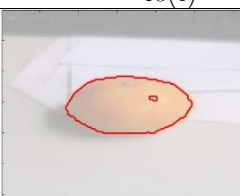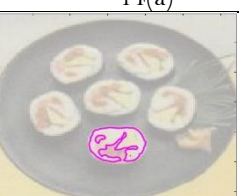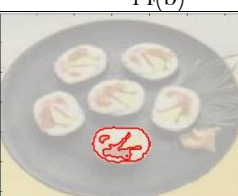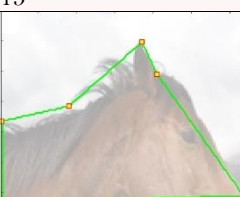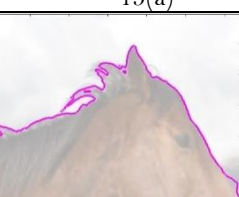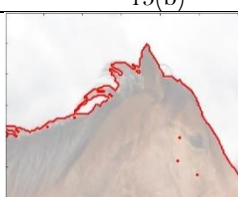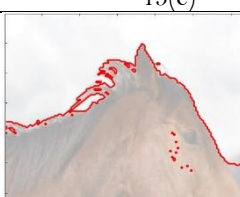
In this section, the overall results of the study are presented. The segmentation performance of the proposed model is compared with that of the existing DSS2 and SSGR models to highlight the differences and effectiveness of the new approach. A total of 16 real vector-valued test images were used in the experiments to segment the specified objects. The dataset and benchmark from Pham [29]; Jizhizi, et al. [30]; Qiao, et al. [31]; Li, et al. [32] and Chen, et al. [33] served as the source of test images. These images were particularly challenging to segment due to intensity inhomogeneity and irregular boundaries. For the qualitative analysis, visual observation was employed to evaluate the segmentation accuracy of the models across all 16 test images. For the quantitative analysis, accuracy, error, JSC, and DSC values were calculated for each model on test images 1 through 16. The segmentation experiments were carried out using the DSS2, SSGR, and SSHI models, and the results are summarized in Table 1.

Table 1. The test images and the segmentation results of the DSS2, SSGR, and SSHI models.

Test Image	DSS2	SSGR	SSHI
1	1(a)	1(b)	1(c)
2	2(a)	2(b)	2(c)
3	3(a)	3(b)	3(c)

4	4(a)	4(b)	4(c)
5	5(a)	5(b)	5(c)
6	6(a)	6(b)	6(c)
7	7(a)	7(b)	7(c)
8	8(a)	8(b)	8(c)
9	9(a)	9(b)	9(c)
10	10(a)	10(b)	10(c)

The first column of Table 1 presents the test images along with their initial segmentation contours, while the second, third, and fourth columns display the final segmentation results obtained from the DSS2, SSGR, and SSHI models, respectively. From visual observation, all models effectively segmented the specific object of interest, even when the color images were hazy. However, closer inspection showed that for test images 1, 4, and 5, the results produced by DSS2 and SSGR were undersegmented, with some regions of the images not captured accurately, whereas the results generated by the proposed SSHI model were improved. Another notable case is test image 9, where the SSHI model successfully segmented the detailed boundaries of the bird's feathers, outperforming both the

DSS2 and SSGR models. To further evaluate the effectiveness of the three models quantitatively, the average values of JSC, DSC, ACC, and Error for each model are reported in Table 2 and Figure 1.

Table 2. Average JSC, DSC, ACC, and Error values for the DSS2, SSGR, and SSHI models in segmenting vector-valued images with haze.

	DSS2	SSGR	SSHI
JSC	0.7121	0.6996	0.7636
DSC	0.8034	0.8064	0.8583
ACC	0.9543	0.9535	0.9616
Error	0.0458	0.0465	0.0384
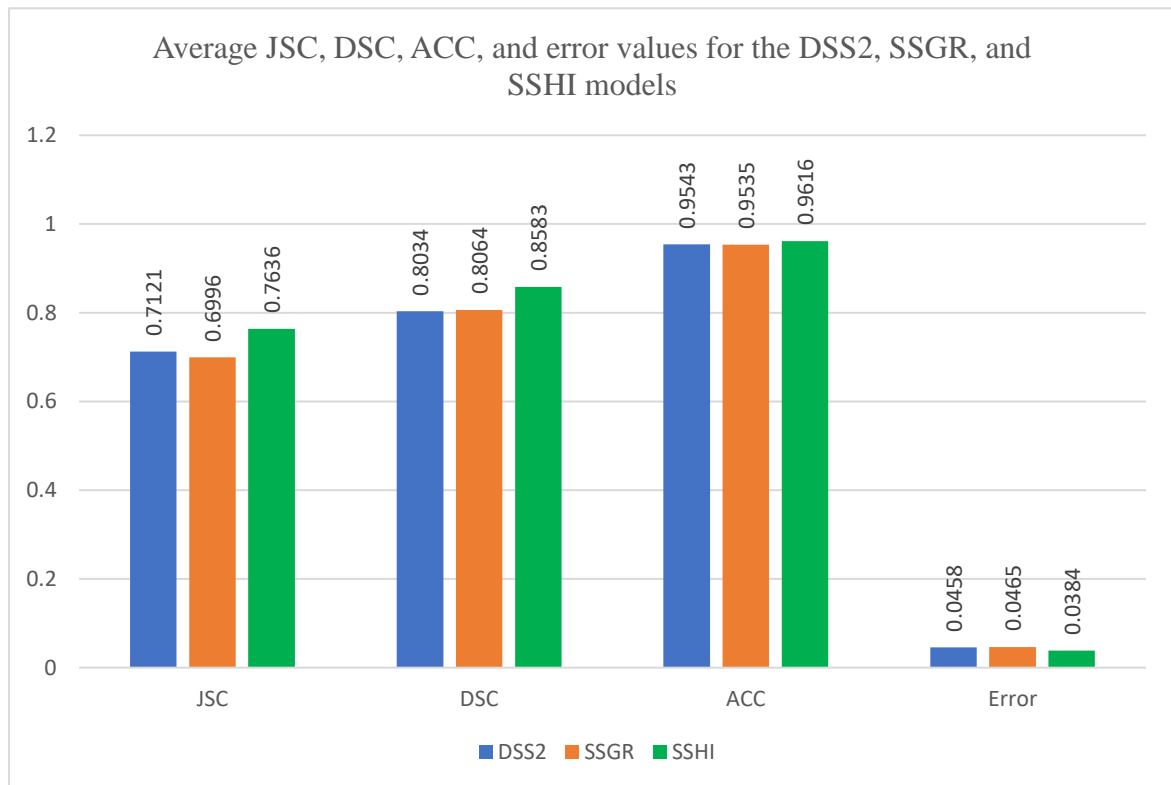
Figure 1. Bar Chart of JSC, DSC, ACC, and Error values for the DSS2, SSGR, and SSHI models in segmenting vector-valued images with haze.

Table 2 reports the numerical values of the four quantitative segmentation metrics namely JSC, DSC, ACC, and Error for the DSS2, SSGR, and the proposed SSHI models. Figure 1 visualizes these same results in the form of a bar chart, offering a clearer comparison across the models and enabling easier interpretation of performance differences. Together, the tabulated and graphical results highlight the consistent improvement of the SSHI model across all metrics, particularly in handling hazy, vector-valued images.

In terms of the JSC, SSHI achieved a score of 0.7636, representing a 7.2% improvement over DSS2 (0.7121) and a 9.1% improvement over SSGR (0.6996). For the Dice Similarity Coefficient (DSC), SSHI obtained 0.8583, outperforming DSS2 (0.8034) by 6.8% and SSGR (0.8064) by 6.4%, demonstrating its stronger capability in boundary delineation. The ACC values further confirm this trend. SSHI recorded 0.9616, which is 0.8% higher than DSS2 (0.9543) and 0.9% higher than SSGR (0.9535). Although the margin is smaller, such improvements are notable since ACC reflects global pixel-level correctness across the entire image. The most substantial gain is observed in the error rate, where SSHI achieved the lowest value at 0.0384. This represents a 16.2% reduction compared to DSS2 (0.0458) and a 17.4% reduction compared to SSGR (0.0465), highlighting SSHI's ability to minimize false assignments under challenging hazy conditions. To verify the reliability of the improvements achieved by the SSHI model, statistical testing was applied to the results obtained from the 16 test images. The Wilcoxon signed-rank test was chosen

because it is a non-parametric approach that does not require the data to follow a normal distribution, and it is suitable for comparing paired values. The comparison was made between the proposed SSHI model and the two baseline methods, DSS2 and SSGR. In the testing, the expectation was that SSHI would produce larger values of JSC, DSC, and ACC, while for Error, the opposite was expected.

The outcomes of the Wilcoxon test supported the advantage of SSHI. For the JSC measure, SSHI obtained significantly higher results than DSS2 (test statistic = 118.0, p = 0.0038) and also than SSGR (test statistic = 136.0, p = 1.53×10^{-5}). This indicates that SSHI provided better boundary separation when haze was present. In terms of DSC, the SSHI scores were likewise greater than those of DSS2 (test statistic = 133.0, p = 7.63×10^{-5}) and SSGR (test statistic = 120.0, p = 3.27×10^{-4}), which suggests improved overlap with the expected segmentation.

For the ACC measure, SSHI again performed better, giving significantly higher values compared to DSS2 (test statistic = 126.5, p = 6.56×10^{-4}) and SSGR (test statistic = 136.0, p = 1.53×10^{-5}). Although the difference was not as large as for JSC and DSC, the improvement was still statistically reliable. On the other hand, for the Error metric, SSHI obtained clearly smaller values. The differences were significant when compared with DSS2 (test statistic = 9.0, p = 5.04×10^{-4}) and with SSGR (test statistic = 0.0, p = 3.27×10^{-4}). This result confirms that SSHI reduced the number of incorrectly classified pixels more effectively than the baseline models.

The p-values (p< 0.01) indicate that the improvements of SSHI compared with DSS2 and SSGR are statistically significant. This suggests that the better results are not only caused by random variation but are attributable to the advantage of the SSHI model itself. Overall, the Wilcoxon test results demonstrate that SSHI provides stable and clear improvements over DSS2 and SSGR across all tested measures. These results also show that incorporating Non-Local Dehazing into the selective segmentation method offers a valuable and reliable gain in accuracy and error reduction when working with hazy vector-valued images. Such improvements are particularly important for real-world applications where visual clarity is compromised, including remote sensing, medical imaging, and environmental monitoring. Next, the efficiency of the proposed model is evaluated. Table 3 and Figure 2 present the average processing time for the DSS2, SSGR, and SSHI models in segmenting vector-valued images with haze.

Table 3. Average processing time (in seconds) for the DSS2, SSGR, and SSHI models in segmenting vector-valued images with haze.

	DSS2	SSGR	SSHI
Average time	7.8587	1.8007	1.6373
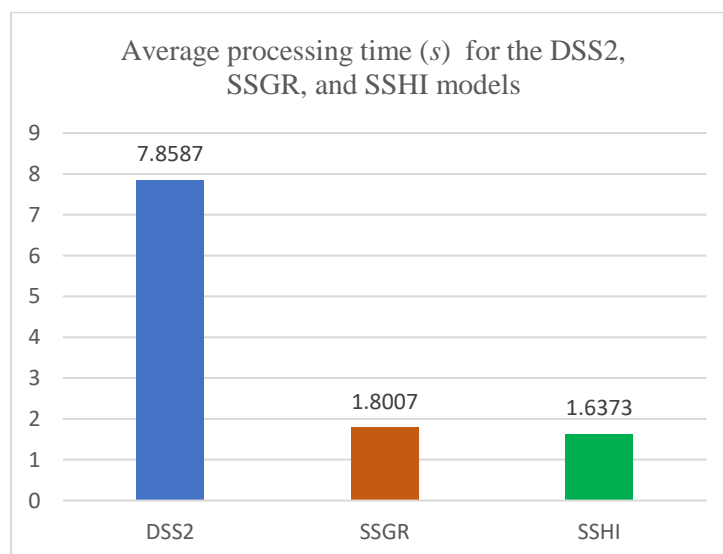
Figure 2. Bar chart of average processing time for the DSS2, SSGR, and SSHI models in segmenting vector-valued images with haze.

294

Table 3 and Figure 2 provide a comparative analysis of the average processing time required by the DSS2, SSGR, and SSHI models when segmenting vector-valued images with haze. While Table 3 reports the exact numerical values, Figure 2 offers a bar chart representation, which facilitates a clearer comparison of computational efficiency among the models. The results demonstrate that the proposed SSHI model achieved the lowest average processing time of 1.6373 s, slightly outperforming SSGR (1.8007 s) and substantially surpassing DSS2 (7.8587 s). This represents a 9.1% improvement over SSGR and a 79.2% reduction in processing time compared to DSS2.

To support these findings, the Wilcoxon signed-rank test was performed with the hypothesis that SSHI requires less time than the baselines. The results showed that SSHI was significantly faster than DSS2. The test produced a statistic of 0.0 with a p-value of 1.53×10^{-5}, confirming that the large reduction in computation time is statistically meaningful. In contrast, when comparing SSHI with SSGR, the difference in time was not statistically significant (test statistic = 42.0, p = 0.0964). This indicates that although SSHI's average execution time was slightly lower than that of SSGR, the variation across test images was not consistent enough to reach significance.

These findings highlight the computational efficiency of the SSHI model. The marginal gain over SSGR underscores SSHI's refinement of the Gaussian-based regularization concept, while the dramatic reduction compared to DSS2 emphasizes the advantages of replacing curvature-dependent formulations with a more efficient structure. The lower processing time, coupled with improved segmentation accuracy (as demonstrated in Table 2 and Figure 1), confirms that SSHI provides an optimal balance between effectiveness and efficiency. Such improvements are particularly valuable in real-world applications, where fast and reliable segmentation of hazy images is required, for example, in real-time surveillance, remote sensing, environmental monitoring, and medical imaging systems, where delays in computation can compromise usability. The limitation of the SSHI model can be observed in the parameter selection approach. In this model, the parameters θ, α_1, and α_2 were chosen by trial and error to achieve good segmentation results, which are difficult and time-consuming.

5. CONCLUSION

This study introduced a new variational selective segmentation model, termed Selective Segmentation for Haze Image (SSHI), designed to address the limitations of existing models when applied to hazy, vector-valued images. By incorporating the Non-Local Image Dehazing technique into the formulation of the SSGR model, SSHI integrates haze removal directly into the segmentation process. Quantitative evaluations on 16 real hazy images, using JSC, DSC, ACC, and Error as performance metrics, demonstrated consistent improvements with SSHI compared to DSS2 and SSGR. The SSHI model achieved higher JSC, DSC, and ACC values, while maintaining the lowest Error rate. Importantly, the Error reduction reached over 16% relative to DSS2 and more than 17% relative to SSGR, indicating enhanced reliability in boundary extraction under challenging imaging conditions. In addition, efficiency analysis revealed that SSHI reduced computational time by approximately 79% compared to DSS2 and achieved a 9% improvement over SSGR. These findings confirm that the integration of image dehazing into the segmentation framework yields both accuracy and efficiency gains. Despite these contributions, the model has certain limitations. Parameter selection was carried out through trial-and-error, a process that is time-consuming. Future work should therefore focus on developing systematic or adaptive parameter estimation strategies such as grid search and Bayesian optimization. Moreover, extending SSHI into three-dimensional formulations and testing its applicability are important directions for further research.

The SSHI model has potential beyond natural images, with relevance to domains such as medical imaging, remote sensing, and environmental monitoring. In these areas, image quality is often degraded by noise or atmospheric effects, and the integration of dehazing within the segmentation process allows clearer boundary extraction. This makes SSHI a practical option in situations where pre-processing or large training datasets are not available.

REFERENCES

[1]   F. A. Shewajo and K. A. Fante, "Tile-based microscopic image processing for malaria screening using a deep learning approach," *BMC Medical Imaging*, vol. 23, no. 1, p. 39, 2023. https://doi.org/10.1186/s12880-023-00993-9

[2]   A. M. Anter and L. Abualigah, "Deep federated machine learning-based optimization methods for liver tumor diagnosis: A review," *Archives of Computational Methods in Engineering*, vol. 30, no. 5, pp. 3359-3378, 2023. https://doi.org/10.1007/s11831-023-09901-4

[3]   S. Srinivasan, P. S. M. Bai, S. K. Mathivanan, V. Muthukumaran, J. C. Babu, and L. Vilcekova, "Grade classification of tumors from brain magnetic resonance images using a deep learning technique," *Diagnostics*, vol. 13, no. 6, p. 1153, 2023. https://doi.org/10.3390/diagnostics13061153

[4]   Z. Q. Habeeb, B. Vuksanovic, and I. Q. Al-Zaydi, "Breast cancer detection using image processing and machine learning," *Journal of Image and Graphics*, vol. 11, no. 1, pp. 1-8, 2023. https://doi.org/10.18178/joig.11.1.1-8

[5]   I. Mishra, K. Aravinda, J. A. Kumar, C. Keerthi, R. D. Shree, and S. Srikumar, "Medical imaging using signal processing: A comprehensive review," presented at the 2022 Second International Conference on Artificial Intelligence and Smart Energy (ICAIS), IEEE, 2022, pp. 623-630.

[6]   Y. M. İkbal and S. Göncü, "Recognition of hereford and simmental cattle breeds via computer vision," *Iranian Journal of Applied Animal Science*, vol. 13, no. 1, pp. 21-32, 2023.

[7]   J. Fang, H. Liu, L. Zhang, J. Liu, and H. Liu, "Region-edge-based active contours driven by hybrid and local fuzzy region-based energy for image segmentation," *Information Sciences*, vol. 546, pp. 397-419, 2021. https://doi.org/10.1016/j.ins.2020.08.078

[8]   N. A. S. Mohd Ghani and A. K. Jumaat, "Selective segmentation model for vector-valued images," *Journal of Information and Communication Technology*, vol. 21, no. 2, pp. 149-173, 2022.

[9]   N. F. Azman *et al.*, "Digital medical images segmentation by active contour model based on the signed pressure force function," *Journal of Information and Communication Technology*, vol. 23, no. 3, pp. 393-419, 2024.

[10]   J. Gu, Z. Fang, Y. Gao, and F. Tian, "Segmentation of coronary arteries images using global feature embedded network with active contour loss," *Computerized Medical Imaging and Graphics*, vol. 86, p. 101799, 2020. https://doi.org/10.1016/j.compmedimag.2020.101799

[11]   Y. Yang, W. Jia, and B. Wu, "Simultaneous segmentation and correction model for color medical and natural images with intensity inhomogeneity," *The Visual Computer*, vol. 36, no. 4, pp. 717-731, 2020. https://doi.org/10.1007/s00371-019-01651-4

[12]   E. Iqbal, A. Niaz, A. A. Memon, U. Asim, and K. N. Choi, "Saliency-driven active contour model for image segmentation," *IEEE Access*, vol. 8, pp. 208978-208991, 2020. https://doi.org/10.1109/ACCESS.2020.3038945

[13]   X.-H. Zhi and H.-B. Shen, "Saliency driven region-edge-based top down level set evolution reveals the asynchronous focus in image segmentation," *Pattern Recognition*, vol. 80, pp. 241-255, 2018. https://doi.org/10.1016/j.patcog.2018.03.010

[14]   N. F. Idris, M. A. Ismail, M. S. Mohamad, S. Kasim, Z. Zakaria, and T. Sutikno, "Breast cancer disease classification using fuzzy-ID3 algorithm based on association function," *IAES International Journal of Artificial Intelligence (IJ-AI)*, vol. 11, no. 2, pp. 448-461, 2022. https://doi.org/10.11591/ijai.v11.i2.pp448-461

[15]   H. M. Ahmed and M. Y. Kashmola, "A proposed architecture for convolutional neural networks to detect skin cancers," *IAES International Journal of Artificial Intelligence (IJ-AI)*, vol. 11, no. 2, pp. 485-493, 2022. http://doi.org/10.11591/ijai.v11.i2.pp485-493

[16]   A. H. T. Al-Ghrairi, A. A. Mohammed, and E. Z. Sameen, "Face detection and recognition with 180 degree rotation based on principal component analysis algorithm," *IAES International Journal of Artificial Intelligence (IJ-AI)*, vol. 11, no. 2, pp. 593–602, 2022. https://doi.org/10.11591/ijai.v11.i2.pp593-602.

[17]   M. Z. Ansari, T. Ahmad, M. M. S. Beg, and N. Bari, "Language lexicons for Hindi-English multilingual text processing," *IAES International Journal of Artificial Intelligence (IJ-AI)*, vol. 11, no. 2, pp. 641–648, 2022. https://doi.org/10.11591/ijai.v11.i2.pp641-648

[18]   N. Badshah and K. Chen, "Image selective segmentation under geometrical constraints using an active contour approach," *Communications in Computational Physics*, vol. 7, no. 4, pp. 759–778, 2010. https://doi.org/10.4208/cicp.2009.09.026

[19]   T. N. A. Nguyen, J. Cai, J. Zhang, and J. Zheng, "Robust interactive image segmentation using convex active contours," *IEEE Transactions on Image Processing*, vol. 21, no. 8, pp. 3734-3743, 2012. https://doi.org/10.1109/TIP.2012.2191566

[20]   L. Rada and K. Chen, "Improved selective segmentation model using one level-set," *Journal of Algorithms & Computational Technology*, vol. 7, no. 4, pp. 509-540, 2013. https://doi.org/10.1260/1748-3018.7.4.509

[21]   J. Spencer and K. Chen, "A convex and selective variational model for image segmentation," *Communications in Mathematical Sciences*, vol. 13, no. 6, pp. 1453-1472, 2015. https://doi.org/10.4310/CMS.2015.v13.n6.a5

[22]   A. K. Jumaat, R. Nithya, and M. M. Kumar, "Gaussian regularization based active contour model for extraction of shape boundaries in vector valued images," *International Journal of Emerging Technology and Advanced Engineering*, vol. 12, no. 9, pp. 102-112, 2022. https://doi.org/10.46338/ijetae0922_11

[23]   H. Ali, A. Sher, M. Saeed, and L. Rada, "Active contour image segmentation model with de-hazing constraints," *IET Image Processing*, vol. 14, no. 5, pp. 921-928, 2020. https://doi.org/10.1049/iet-ipr.2018.5987

[24]   D. Berman and S. Avidan, "Non-local image dehazing," in *Proceedings of the IEEE Conference on Computer Vision and Pattern Recognition*, 2016, pp. 1674-1682.

[25]   S. Lee, T. Son, and S. Kwak, "Fifo: Learning fog-invariant features for foggy scene segmentation," in *Proceedings of the IEEE/CVF Conference on Computer Vision and Pattern Recognition*, 2022, pp. 18911-18921.

[26]   Q. Bi, S. You, and T. Gevers, "Generalized foggy-scene semantic segmentation by frequency decoupling," in *Proceedings of the IEEE/CVF Conference on Computer Vision and Pattern Recognition*, 2024, pp. 1389-1399.

[27]   Q. Bi, S. You, and T. Gevers, "Learning generalized segmentation for foggy-scenes by Bi-directional wavelet guidance," *Proceedings of the AAAI Conference on Artificial Intelligence*, vol. 38, no. 2, pp. 801-809, 2024. https://doi.org/10.1609/aaai.v38i2.27838

[28]   M. Lee, K. Song, and J. Choe, "Fog-free training for foggy scene understanding," *Pattern Recognition Letters*, vol. 189, pp. 129-135, 2025. https://doi.org/10.1016/j.patrec.2025.01.012

[29]   V.   T.   Pham,   "How   to   use   Detectron2,"   github.com,"   Retrieved: https://github.com/facebookresearch/detectron2/issues/795. [Accessed Feb. 5], 2024.

[30]   L. Jizhizi, J. Zhang, and D. Tao, "Deep automatic natural image matting," in *Proceedings of the 30th International Joint Conference on Artificial Intelligence*, 2021.

[31]   Y. Qiao *et al.*, "Attention-guided hierarchical structure aggregation for image matting," in *Proceedings of the IEEE/CVF Conference on Computer Vision and Pattern Recognition*, 2020, pp. 13676-13685.

[32]   H. Li, J. Cai, T. N. A. Nguyen, and J. Zheng, "A benchmark for semantic image segmentation," in *2013 IEEE International Conference on Multimedia and Expo, IEEE*, 2013, pp. 1-6.

[33]   M.-Y. Chen *et al.*, "Automatic Chinese food identification and quantity estimation," in SIGGRAPH Asia 2012 Technical Briefs." Taiwan: National Taiwan University, 2012.